Ab initio prediction of anomalous Hall effect in antiferromagnetic $CaCrO_3$

Thi Phuong Thao Nguyen and Kunihiko Yamauchi
Institute of Scientific and Industrial Research, Osaka University, 8-1 Mihogaoka, Ibaraki, Osaka, 567-0047, Japan
and Department of Precision Engineering, Graduate School of Engineering,
Osaka University, 2-1 Yamadaoka, Suita, Osaka 565-0871, Japan

(Received 25 January 2023; revised 28 March 2023; accepted 29 March 2023; published 13 April 2023)

While the anomalous Hall effect takes place typically in ferromagnets with finite magnetization, large anomalous Hall conductivity in *noncollinear* antiferromagnetic systems has been recently observed and attracted much attention. In this paper, we predict the anomalous Hall effect in perovskite $CaCrO_3$ as a representative of *collinear* antiferromagnetic materials. Our result shows that the *C*-type antiferromagnetic ordering generates the sizable anomalous Hall conductivity. Based on symmetry analyses, we show that the antiferromagnetic order parameter belongs to the same irreducible representation as the ferromagnetic order parameter in the nonsymmorphic space group, allowing the nonvanishing Berry curvatures in k space. By performing first-principles density-functional theory calculations, we find that the Berry-curvature "*hot spots*" lie along the gapped nodal lines where spin-orbit coupling induces the spin splitting of Cr-3*d* bands near the Fermi energy and enhances the anomalous Hall effect in $CaCrO_3$.

DOI: 10.1103/PhysRevB.107.155126

I. INTRODUCTION

The anomalous Hall effect (AHE) is traditionally considered to be proportional to net magnetization and, therefore, appears only in ferromagnetic (FM) materials [1]. Nevertheless, recent studies have revealed that large anomalous Hall conductivity (AHC) emerges in Kagome antiferromagnetic (AFM) materials, such as Mn_3Ge and Mn_3Sn regardless of their small net magnetization [2–10]. Such a large AHC in antiferromagnets may work as a readout for a spintronic device accompanied by their ultrafast spin dynamics and insensitivity to external magnetic fields, whereas only a few AFM materials have been studied in this context [11–15].

Suzuki *et al.* have investigated the magnetic symmetry by introducing a magnetic cluster extension; the noncollinear AFM structure in Mn_3Sn is characterized by the cluster octupole moment, which belongs to the same irreducible representation as the collinear ferromagnetic ordering. This explains why the noncollinear antiferromagnetic order can induce an AHC despite its vanishingly small dipole magnetization [16]. The same approach has been later applied to antiperovskite manganese nitrides, such as Mn_3PtN, where their magnetic octupole noncollinear AFM states allow for inducing the large AHC as well [17].

Recent theoretical development provides the topological formulation of the intrinsic AHE in terms of the Berry phase associated with the Bloch wave functions in solids [18]. While the AHC can be calculated by integrating the Berry curvature in the Brillouin zone, the computation is practically demanding because the Berry curvature in many cases a very sharply varying function of the k vector. It often strongly depends on contributions from a few "*hot spots*" in the k space where the spin-orbit-coupling (SOC) causes anticrossing between bands near the Fermi energy. Such features often require an extremely dense k-point sampling, and for this reason, the Wannier functions are employed to interpolate the band structure and the wave functions [18]. In Mn_3Sn, the Berry curvature stemming from the Weyl points enhances AHC in the absence of net magnetization [10]. In contrast, in Mn_3PtN, the Berry curvatures spread around the Fermi surfaces in the broad Brillouin-zone region, coming from the band splitting due to the SOC, dominantly contributes to the AHC [17].

Very recently, Naka *et al.* have theoretically examined the possibility of the AHE in perovskite transition-metal oxides [19]. It has been predicted that the coexistence of the $GdFeO_3$-type structural distortion and the collinear AFM configuration gives rise to the AHE by means of the Hubbard model. One of the candidate materials proposed is $CaCrO_3$, which is a rare example of a metallic and antiferromagnetic transition-metal oxide. $CaCrO_3$ crystallizes in orthorhombic *Pbnm* (alternative setting of *Pnma*) perovskite structure. Although $CaCrO_3$ was previously reported to show semiconducting [20] or insulating [21] properties with the AFM order, recent works have reported its metallic conductivity below the Néel temperature $T_N = 90$ K [22,23]. Powder neutron-diffraction analysis and μSR measurement have revealed that the AFM spin structure is *C*-type AFM (*C*-AFM) in which Cr spins order antiferromagnetically on the *ab* plane but ferromagnetically along the c axis [24,25]. Owing to the orthorhombic lattice distortion with the metallic collinear AFM ground state, $CaCrO_3$ is a suitable playground to realize the AHE with no need to consider the complex magnetism, such as spin chirality and/or magnetic multipole configurations. In this paper, we perform density-functional theory (DFT) calculations to evaluate the AHC in $CaCrO_3$ and discuss its microscopic mechanism along with the magnetic symmetry analysis.

II. METHODOLOGY

DFT calculations were performed by using VASP [26] and QUANTUM ESPRESSO [27] packages. The generalized gradient approximation (GGA) with the parametrization of Perdew, Burke, and Ernzerhof [28] was used for the exchange-correlation functional. The calculations were carried out by the following steps. First, the atomic structure was optimized with the C-AFM configuration until the atomic force become lower than 0.001 eV/Å using the VASP code with the projector augmented-wave pseudopotential [29], and then the electronic structure and the magnetic stability were investigated. Second, another self-consistency calculation was performed by using the QUANTUM ESPRESSO code with the fully relativistic ultrasoft pseudopotentials [30]. The kinetic-energy cutoff of 80 and 800 Ry were used for the plane-wave basis set and charge density, respectively. A $12 \times 12 \times 10$ k-point mesh was taken in the Brillouin zone with the tetrahedron method for integration. Third, we constructed maximally localized Wannier functions by using the WANNIER90 code [31] that is interfaced with the QUANTUM ESPRESSO code. The Wannier functions were built by projections of Bloch wave functions onto the localized Cr-3d orbital basis; there are 40 d orbital states in the C-AFM unit cell (4 f.u.). These atomic orbital functions must be carefully chosen otherwise the maximally localization process of the Wannier functions does not converge well. We set up the local (x, y, z) axes in the CrO_6 octahedron by considering the Cr-O bond directions to satisfy the condition: z is parallel to the long bond, x is parallel to the short bond, and y is parallel to the middle bond. The angular functions, $3z^2 - r^2$, zx, yz, $x^2 - y^2$, and xy, were defined in the local coordinates for the Wannier projection. After the Wannier functions were maximally localized, we finally calculated the Berry curvature and the AHC with $120 \times 120 \times 100$ k-point mesh with $5 \times 5 \times 5$ adaptive mesh refinement for the turbulent regions.

III. RESULTS AND DISCUSSIONS

A. Electronic and magnetic properties

Figure 1 shows the *Pbnm* crystal structure of $CaCrO_3$ with the orthorhombic Brillouin zone and the calculated electronic structure. The metallic state is clearly exhibited by the 2/3-filled Cr-t_{2g} state crossing the Fermi energy. Since the t_{2g} level is located away from the O-p level, and the threefold degeneracy is not completely lifted due to the lack of strong Jahn-Teller distortion, the t_{2g} state has a rather localized character and forms the flat bands in the vicinity of the Fermi level. It also appears as a sharp peak, the so-called van Hove singularity in the DOS being responsible for the high electric conductivity. In contrast, the e_g orbital state shows a delocalized character as strongly hybridizing with the O-p state. The e_g-p bonding state lies in a wide energy range below t_{2g} state and the antibonding state spreads above the t_{2g} state. The trend is consistent with the previous DFT works [32,33].

The nonmagnetic *Pbnm* space group has eight symmetry operations: $\{E,\ I,\ C_{2x} + (\frac{1}{2}\frac{1}{2}0),\ C_{2y} + (\frac{1}{2}\frac{1}{2}\frac{1}{2}),\ C_{2z} + (00\frac{1}{2}),\ m_x + (\frac{1}{2}\frac{1}{2}0),\ m_y + (\frac{1}{2}\frac{1}{2}\frac{1}{2}),\ m_z + (00\frac{1}{2})\}$, where E, I, C, and m denote identity, inversion, rotation, and mirror operations, respectively. Three screw and two glide symmetries involving fractional translations manifest the nonsymmorphic space group.

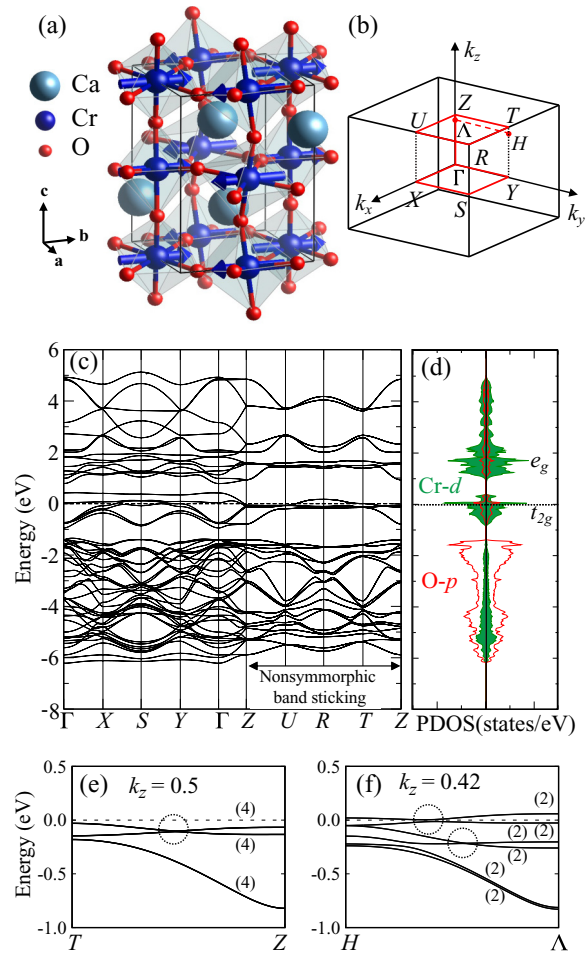

FIG. 1. (a) Orthorhombic *Pbnm* crystal structure of $CaCrO_3$ with the C-AFM spin configuration with Cr spins set parallel to the y axis. (b) First Brillouin zone with the high-symmetry points. (c) Calculated band structure with the C-AFM configuration without SOC. (d) Corresponding density of states (DOS) projected on Cr-d (filled green) and O-p (red) orbital states. (e) and (f) The band structure near the Fermi energy along the $T - Z$ line and the H-Λ line at k_z=0.42, respectively. The number in parentheses is the degeneracy for the band. Fermi energy is set at zero.

The nonsymmorphic group operations lead to band degeneracies, so-called "*band sticking*," across an entire face of the Brillouin zone [34,35]. Figure 1(c) illustrates the band-sticking effect on the $k_z = 0.5$ plane. Under the C-AFM configuration, all the bands are spin degenerate at the high-symmetric k points, and the additional band-sticking degeneracy is imposed at the Brillouin-zone surfaces. Therefore, twofold 12 t_{2g} bands become fourfold six bands on the $Z - U - R - T$ plane [also see Fig. 2(a)]. The sticking effect causes a narrow bunch of bands just below the Fermi energy along the $T - Z$ line at the $k_z = 0.5$ plane [Fig. 1(e)]. Along the $H - \Lambda$ line at the $k_z = 0.42$ plane, they are split into two groups, and the upper-lying bands manifest the band crossing exactly at the Fermi energy [Fig. 1(f)], forming the nodal lines that will be important later in a following section. Figure 2 shows the band structure projected onto Cr-d orbital states and

TABLE I. Transformation properties in nonmagnetic space-group $Pbnm1'$ for FM (F_α) and AFM (A_α, C_α, and G_α) magnetic ordering parameters with $\alpha = x, y, z$ components in the global frame. Only the generators of symmetry operations are shown. The group elements denote the identity, two screws, the inversion, and the time reversal. Irreducible representation's (IR's) name is taken from ISODISTORT software [39].

IR of $Pbnm1'$	E	$C_{2x} + (\frac{1}{2}\frac{1}{2}0)$	$C_{2y} + (\frac{1}{2}\frac{1}{2}\frac{1}{2})$	I	θ	Nonzero M component	Nonzero AHC component	Magnetic space group
$m\Gamma_1$: A_x, C_z, G_y	1	1	1	1	−1			$Pbnm$
$m\Gamma_2$: F_x, C_y, G_z	1	1	−1	1	−1	M_x	σ_{yz}	$Pbn'm'$
$m\Gamma_3$: F_y, A_z, C_x	1	−1	1	1	−1	M_y	σ_{zx}	$Pb'nm'$
$m\Gamma_4$: F_z, A_y, G_x	1	−1	−1	1	−1	M_z	σ_{xy}	$Pb'n'm$

the Fermi surfaces obtained by using the Wannier-function interpolation. The t_{2g} orbital states are split into xy and $(zx \pm yz)$ orbital states; the latter is a linear combination of two orbital states at neighboring Cr sites. Among them, 5–6th and 7–8th bands form the hole Fermi-surface pockets around the $R-S$ line and 9–10th and 11–12th bands form the lotus-leaf-shaped flat electron Fermi surfaces near the $k_z = 0.5$ plane.

The magnetic stability was examined by comparing the total energy between several magnetic configurations. It is found that C-AFM order shows the total energy lower than those of other spin configurations: FM, A-type AFM, and G-type AFM by 209.2, 59.4, and 103.9 meV/f.u, respectively. Taking into account the SOC, it is also found that C-AFM order shows the magnetic easy axis along the global y direction. The energy difference is 0.76 and 0.98 meV/f.u. with respect to the energy with the x and the z spin directions, respectively. Since the magnetic anisotropy energy is very small, hereinafter, we will examine the AHC in the C-AFM configuration with spins ordered along the x, y, and z axes to compare the values. Then, we will focus on the C-AFM order with the y spin orientation to investigate the origin of the AHC in more detail.

B. Magnetic symmetry analysis

When the SOC is involved under the magnetic configuration, the crystalline symmetry is lowered, and we must introduce the magnetic space group considering the specified spin direction. In Table I, we show the transformation rules in the nonmagnetic space-group $Pbnm1'$ considering FM (F), A-type AFM (A), C-type AFM (C), and G-type AFM (G) order parameters with (x, y, z) spin orientation; e.g., C_y indicates the C-AFM order in which the spins are parallel along the global y axis. It is shown that three magnetic order parameters belong to the same irreducible representation, i.e., $\{F_x, C_y, G_z\}$ orders belong to $m\Gamma_2$. It implies that the C_y spin configuration is allowed to cause weak-ferromagnetic spin canting toward the x direction and weak-antiferromagnetic spin canting with the G_z spin component without further symmetry reduction as being consistent with earlier symmetry analyses in Refs. [36–38]. This is also consistent with an experimental observation of the C_y ground state with the F_x-type weak ferromagnetism in Ref. [24]. In addition, it must be noted that the magnetic symmetry allows the finite AHC in the C_y or G_z order as well as in the F_x order even if the net magnetization is negligible. This is because the physical properties of those three magnetic orders can be regarded equivalent from a symmetry point of view. This unusual symmetry property that the AFM order and the FM order share the same irreducible representation comes from the nonsymmorphic symmetry operations. For instance, $C_{2x} + (\frac{1}{2}\frac{1}{2}0)$ screw operation flips the y and z spin components located at (000) site and transfers it to the $(\frac{1}{2}\frac{1}{2}0)$ site. The transfer between different spin sublattices in the C-AFM configuration makes C_y order invariant under the screw operation as it makes the F_x order invariant as well. The symmetry analysis here is also consistent with previous theoretical work on orthorhombic $LaCrO_3$ in which the finite FM orbital magnetization and the optical nonreciprocity were predicted in the AFM configurations [38].

The magnetic space group under $\{F_x, C_y, G_z\}$ order is type III $Pbn'm'$ ($Pn'm'a$ in the standard setting), containing four unitary operations $\{E, I, C_{2x} + (\frac{1}{2}\frac{1}{2}0), m_x + (\frac{1}{2}\frac{1}{2}0)\}$ and four antiunitary operations $\{C_{2y}\theta + (\frac{1}{2}\frac{1}{2}\frac{1}{2}), C_{2z}\theta + (00\frac{1}{2}), m_y\theta + (\frac{1}{2}\frac{1}{2}\frac{1}{2}), m_z\theta + (00\frac{1}{2})\}$, where θ denotes the antiunitary time-reversal operator.

C. Anomalous Hall conductivity

The AHC was calculated as integrating the Berry curvatures with a summation over the occupied states in the Brillouin zone by the WANNIER90 code [31,40],

$$\sigma_{\alpha\beta} = -\frac{e^2}{\hbar}\int_{\mathrm{BZ}} \frac{d\boldsymbol{k}}{(2\pi)^3} \sum_n f_n(\boldsymbol{k})\Omega_{n,\alpha\beta}(\boldsymbol{k}), \tag{1}$$

where n is the band index, α and β are the global Cartesian directions (x, y, z); $\alpha \neq \beta$ for the AHC components, and $f_n(\boldsymbol{k})$ is the occupation factors at the $\boldsymbol{k}$ point. The Berry curvature was calculated by

$$\Omega_{n,\alpha\beta}(\boldsymbol{k}) = -2\,\mathrm{Im}\langle\nabla_{k_\alpha} u_{n\boldsymbol{k}}|\nabla_{k_\beta} u_{n\boldsymbol{k}}\rangle, \tag{2}$$

in the WANNIER90 code [31,41]. Here, $u_{n\boldsymbol{k}}$ is the cell-periodic Bloch functions for the nth band, projected onto Wannier functions $|\boldsymbol{R}n\rangle$ by

$$u_{n\boldsymbol{k}} = \sum_{\boldsymbol{R}} e^{-i\boldsymbol{k}\cdot(\boldsymbol{r}-\boldsymbol{R})}|\boldsymbol{R}n\rangle. \tag{3}$$

By applying the conventional perturbation theory, the Berry curvature can be cast into the form of a Kubo-like formula,

$$\Omega_{n,\alpha\beta}(\boldsymbol{k}) = -2\hbar^2\mathrm{Im}\sum_{m\neq n} \frac{v_{nm,\alpha}(\boldsymbol{k})v_{mn,\beta}(\boldsymbol{k})}{[\epsilon_m(\boldsymbol{k}) - \epsilon_n(\boldsymbol{k})]^2}, \tag{4}$$

where $\epsilon_n(\boldsymbol{k})$ is the eigenenergy for the nth band at a given $\boldsymbol{k}$ point and $v_{nm,\alpha}(\boldsymbol{k})$ is the matrix element of

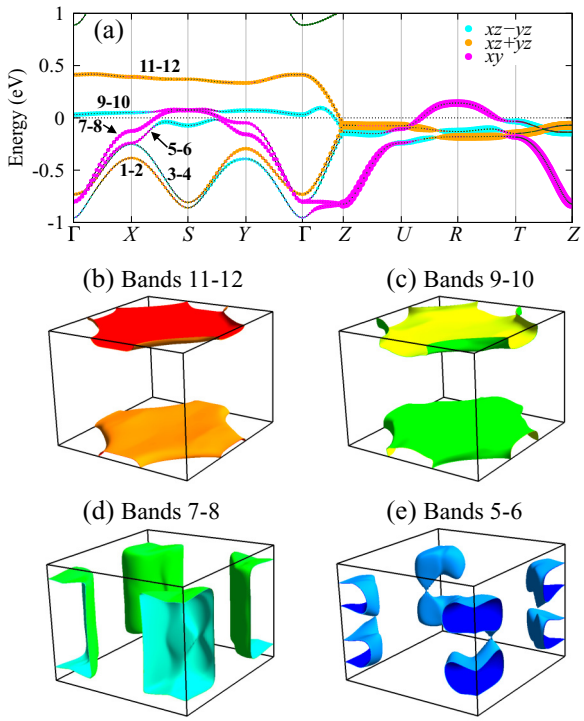

FIG. 2. (a) Wannier-interpolated band structure under the C-AFM configuration projected onto Cr-d orbital states without taking into account the SOC. The band number reflects the AFM spin degeneracy. The colors highlight the following d-orbital components; magenta denotes d_{xy}, orange denotes d_{zx+yz}, and cyan denotes d_{zx-yz} states. The radii of the circles are proportional to the weights of corresponding orbital states. Fermi energy is set at zero. (b)–(e) Calculated Fermi surfaces with the corresponding band numbers in the orthorhombic Brillouin zone.

the velocity operator between the occupied n state and the unoccupied m state. The AHC and Berry curvature can be regarded as axial vectors, like the spin momentum under the magnetic symmetry operations in their vector form: $\boldsymbol{\sigma} = (\sigma_x, \sigma_y, \sigma_z) = (\sigma_{yz}, \sigma_{zx}, \sigma_{xy})$ and $\boldsymbol{\Omega} = (\Omega_x, \Omega_y, \Omega_z) = (\Omega_{yz}, \Omega_{zx}, \Omega_{xy})$, where n and k dependencies were omitted for simplicity. Since Ω is odd with respect to time-reversal symmetry flipping the k vector, the summation of Ω and accordingly the AHC are zero for nonmagnetic materials. Similarly, the symmetry operations transforming k to $-k$ and Ω to $-\Omega$ simultaneously, the AHC vanishes. Table II shows the transformation of k and Ω under the $\{F_x, C_y, G_z\}$ order; here only summation of Ω_x in the k space ($=\sigma_x$) can be nonzero, whereas, Ω_y and Ω_z cancel out in summation. All the components of AHC vanish if SOC is not considered in the calculations. In the absence of SOC, the spin direction does not affect the orbital nor charge state and, hence, the spin state is transformed under symmetry operations defined in a black-and-white group (see Appendix A), preventing the spin polarization and the AHC in any direction.

Figure 3 shows the calculated AHC in the C-AFM configuration. All the tensor components were found to be negligible except σ_{yz} in C_y and σ_{zx} in C_x AFM configurations being in agreement with our symmetry analysis (cf. Table I). The values of σ_{yz} and σ_{zx} at Fermi energy were calculated as -74 and -149 S/cm, respectively [42] We obtained the larger AHC value in the FM order; $\sigma_{yz} = -150$ S/cm with the F_x order in $CaCrO_3$. These values are comparable to that in noncollinear AFM Mn_3Sn, reported as $\sigma_{yz}^{\mathrm{DFT}} = 129$ S/cm [16] ($\sigma_{yz}^{\mathrm{EXP}} = 100$ S/cm [6]). Despite the sizable AHC values, $CaCrO_3$ yields only tiny weak-ferromagnetic spin canting with the net magnetization $M_x = 0.03\,\mu_B$/f.u. obtained after optimizing the spin directions in the C_y-AFM configuration. This clearly indicates that the conductive electrons sensitively experience the Berry curvature as a fictitious magnetic field in k space instead of the magnetic field caused by the spontaneous magnetization in real space.

TABLE II. Transformation rules for crystal momentum $\boldsymbol{k}$ and Berry curvature $\boldsymbol{\Omega}$ under symmetry operations in the $Pbn'm'$ magnetic space group under the $\{F_x, C_y, G_z\}$ order. The translation operations in the spiral and glide symmetry operations were removed in the k space.

	$\{k_x, k_y, k_z\}$	$\{\Omega_x, \Omega_y, \Omega_z\}$
E	$\{k_x, k_y, k_z\}$	$\{\Omega_x, \Omega_y, \Omega_z\}$
I	$\{-k_x, -k_y, -k_z\}$	$\{\Omega_x, \Omega_y, \Omega_z\}$
C_{2x}	$\{k_x, -k_y, -k_z\}$	$\{\Omega_x, -\Omega_y, -\Omega_z\}$
m_x	$\{-k_x, k_y, k_z\}$	$\{\Omega_x, -\Omega_y, -\Omega_z\}$
$C_{2y}\theta$	$\{-k_x, k_y, -k_z\}$	$\{\Omega_x, -\Omega_y, \Omega_z\}$
$C_{2z}\theta$	$\{-k_x, -k_y, k_z\}$	$\{\Omega_x, \Omega_y, -\Omega_z\}$
$m_y\theta$	$\{k_x, -k_y, k_z\}$	$\{\Omega_x, -\Omega_y, \Omega_z\}$
$m_z\theta$	$\{k_x, k_y, -k_z\}$	$\{\Omega_x, \Omega_y, -\Omega_z\}$

The nonmonotonous behavior of σ_{yz} and σ_{zx} with respect to the energy is closely associated with the multifold t_{2g} band structure around the Fermi energy, showing a different trend from the result calculated by a tight-binding model showing simpler energy dependency [19]. In fact, by virtue of the Wannier interpolation, we can quantitatively evaluate the magnitude of the AHC that is sensitive to tiny features of the band structure, such as spin-orbit-induced band anti-crossing in a tiny k-space volume. The AHC values can be enhanced by shifting the Fermi energy either upward or downward (see Fig. 3). For example, $\sigma_{yz} = -441$ S/cm at $E = E_F + 36$ meV in the C_y-AFM and $\sigma_{zx} = 363$ S/cm at $E = E_F + 75$ meV

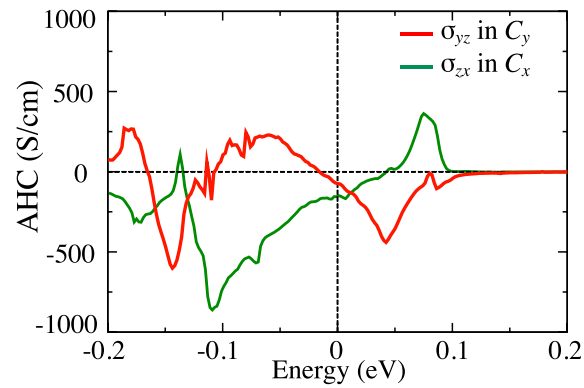

FIG. 3. The calculated AHC tensor components; σ_{yz} in the C_y-AFM configuration and σ_{zx} in the C_x-AFM configuration as functions of energy. Fermi energy is set to zero.

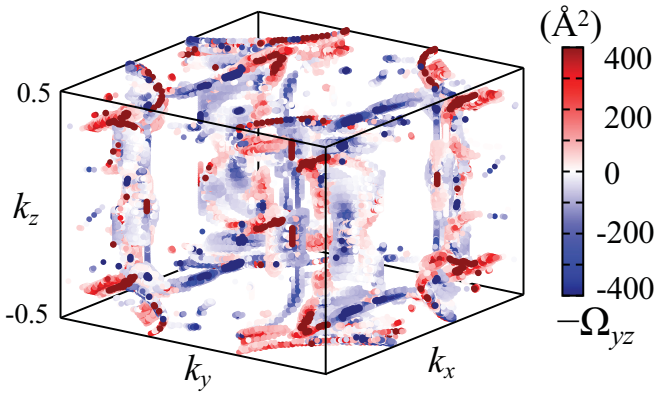

FIG. 4. Distribution of Berry curvatures $-\Omega_{yz}$ (Å^2) over the octahedral Brillouin zone in the C_y-AFM configuration.

in the C_x-AFM configurations. These values are comparable to the AHC value ($\sigma_{xy} \sim 750$ S/cm) calculated in FM bcc Fe [40,43], implying the possible enhancement of the AHC in $CaCrO_3$ via chemical doping in practice.

D. Berry curvature and band splitting

In the following, to clarify the microscopic origin of the sizable AHC, we focus on the C_y-AFM configuration. Figure 4 shows the distribution of the Berry curvatures Ω_{yz} in the orthorhombic Brillouin zone. It can be seen that the shape formed by the high Berry curvature spots resembles some Fermi surfaces [shown in Figs. 2(b)–2(e)] manifesting that the Berry curvatures stem mainly from the topologically nontrivial points in the vicinity of the Fermi surfaces [44,45].

Significantly high Berry curvatures were detected at the $k_z = 0.42$ plane in the Brillouin zone. As shown in Fig. 5(a), the high Berry curvatures plot visualizes the hot spots, i.e., two broad lines running parallel to the k_x axis. These spots are located along the nodal lines opening a small gap near the Fermi energy [cf. Figs. 5(c) and 5(e)] and originating from the interband interaction between the 11th and 12th bands [also see the corresponding Fermi surfaces at Fig. 2(b)].

Although one may think that those two bands (i.e., up- and down-spin polarized bands coming from up- and down-spin Cr sites, respectively) were degenerate in the collinear AFM order, the magnetic symmetry, in fact, allows the spin splitting *even without SOC* at generic k points owing to the effective PT violation; $CaCrO_3$ can be categorized into SST-4A type, like $LaMnO_3$ in Ref. [46]. The spin degeneracy is protected by some symmetry that couples the up-spin and down-spin sites at the higher symmetric k points along the ΛH line (k_x=0.0; $-0.5 < k_y < 0.5$; k_z=0.42) as shown in Fig. 5(b) (for the detail symmetry analysis, see Appendix A). On the other hand, at nonsymmetric k points (k_x=0.1; $-0.5 < k_y < 0.5$; k_z=0.42) shown in Fig. 5(d), the spin degeneracy is lifted even without the SOC.

A couple of the spin-polarized bands are crossing exactly at the Fermi energy, resulting in the nodal lines. When the SOC is turned on, a small gap appears by the anticrossing effect, and the two bands hybridize across the gap through the SOC interaction. This, in turn, lets the bands originally having S_y polarization acquire weak S_x polarization as shown

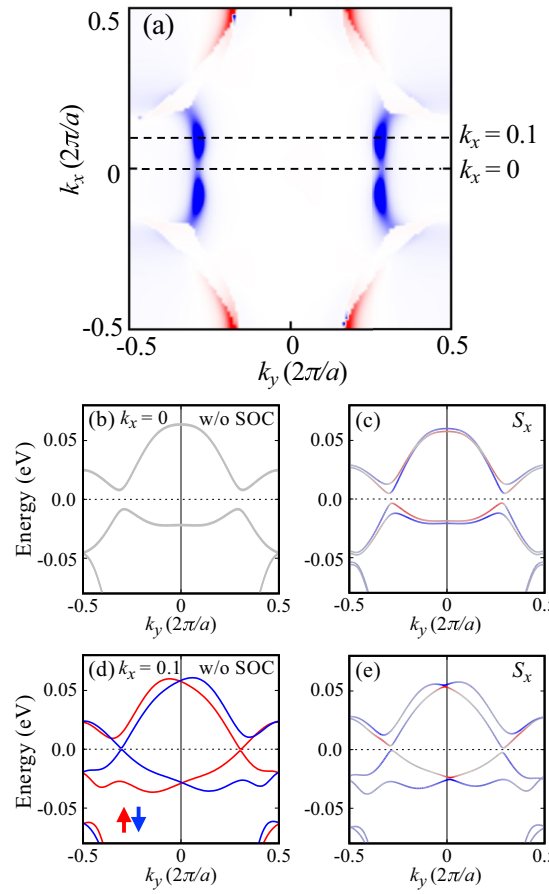

FIG. 5. (a) Color map of the Berry curvature Ω_{yz} on the $k_z = 0.42$ plane under the C_y-AFM configuration. The color range is set same as in Fig. 4. Band structure along the k_y direction corresponding to two dashed lines in (a) on the same plane; (b) and (c) for $k_x = 0$ without the SOC and with the SOC, respectively; (d) and (e) for $k_x = 0.1$ without the SOC and with the SOC, respectively. In (c) and (e), the spin polarization along the x direction (S_x) is shown by red and blue colors. In (d), the spin polarization does not have any preferential direction.

in Fig. 5(e). Simultaneously, Ω_{yz} manifests itself and shows strong enhancement due to the tiny anticrossing gap along the nodal lines due to Eq. (4). In terms of magnetic symmetry, m_x and $m_y\theta$ symmetries keep the Ω_{yz} invariant and makes the hot-spot shape symmetric along the k_x and k_y directions on the plane.

E. Effect of structural distortion on anomalous Hall conductivity

As discussed in the preceding section, the nonsymmorphic symmetry operation that relates the opposite spin sites in the AFM order is a key factor to link the AFM order to the FM order and to give rise to the AHE in collinear AFM materials. The orthorhombic crystal structure of $CaCrO_3$ accommodates a three-dimensional rotation of the octahedra, known as the $GdFeO_3$ rotation, concurrently with a Jahn-Teller distortion with respect to the cubic perovskite structure. Considering that the cubic perovskite structure shows the symmorphic $Pm\bar{3}m$ space group, we can deduce that the $GdFeO_3$ rotation

TABLE III. Optimized lattice constants a, b, and c (Å), Cr-O-Cr bond angle on the CrO_2 plane θ (°), long and short bond distances between Cr and O atoms $d_{\rm long}$ (Å) and $d_{\rm short}$ (Å), and the calculated AHC σ_{yz} (S/cm) at the Fermi energy in $ACrO_3$ for A=Mg, Ca, and Sr under the C_y-AFM order.

	a	b	c	θ	$d_{\rm long}$	$d_{\rm short}$	σ_{yz}
$MgCrO_3$	4.9833	5.1886	7.3030	139.9	1.94	1.91	73.5
$CaCrO_3$	5.2873	5.3566	7.4985	155.2	1.92	1.91	74.8
$SrCrO_3$	5.4245	5.4245	7.6639	180.0	1.91	1.91	0.0

drives the AHE and the resulted AHC increases with the distortion.

In order to examine the effect, we performed additional DFT calculations of the AHC in $MgCrO_3$ and $SrCrO_3$, replacing the A-site cation in $CaCrO_3$ by smaller and larger elements, respectively. The crystal structures were relaxed starting from the $CaCrO_3$structure. Table III summarizes the detail of the relaxed structure and the calculated AHC in $MgCrO_3$, $CaCrO_3$, and $SrCrO_3$. The calculated Cr-O-Cr bond angles show that the $GdFeO_3$-type octahedral tilting is enhanced in $MgCrO_3$ and absent in $SrCrO_3$. This is consistent with an experimental observation that $SrCrO_3$ crystallizes in the tetragonal $P4/mmm$ structure [47]. The resulted AHC shows that σ_{xy} is zero for $SrCrO_3$, and σ_{xy} for $MgCrO_3$ is smaller than that for $CaCrO_3$; the latter is counterintuitive. In fact, the magnitude of the AHC strongly depends on the detail of the band structure near the Fermi energy and, therefore, it is not directly controlled by tuning the structural distortion. Nevertheless, our result highlights the importance of structural distortion as a driving force of the AHE.

IV. SUMMARY

The AHE in $CaCrO_3$ was predicted by means of first-principles calculation supported by symmetry analysis. The AHC was found to be sizable in the collinear C-AFM as the magnetic ground state, and we revealed two essential roles of the nonsymmorphic symmetry. (i) The screw and glide symmetry operations bind the AFM and FM order parameters in the same irreducible representation so that the AHE is active in the AFM order. (ii) The band-sticking effect at the Brillouin-zone surface makes the Cr-t_{2g} state form the narrow bands near the Fermi energy; a couple of those bands cause anticrossing and enhancement of the Berry curvature. We hope that our prediction of the AHE in $CaCrO_3$ will be verified by future experiments. We also expect that our paper will provide an important step forward in the understanding of this unusual AHE and in the exploration of related phenomena further in transition-metal oxides with their wide variety of structures and tunable magnetic properties.

ACKNOWLEDGMENTS

We are grateful to M. Naka, M.-T. Suzuki, and S. Picozzi for the fruitful discussions. This work was supported by JST-CREST (Grant No. JPMJCR18T1). The computation in this paper has been performed using the facilities of the Supercomputer Center, the Institute for Solid State Physics, the University of Tokyo and Supercomputing System MASAMUNE-IMR in the Center for Computational Materials Science, Institute for Materials Research, Tohoku University (Project No. 202112-RDKGE-0046). The crystallographic figure was generated using the VESTA program [48].

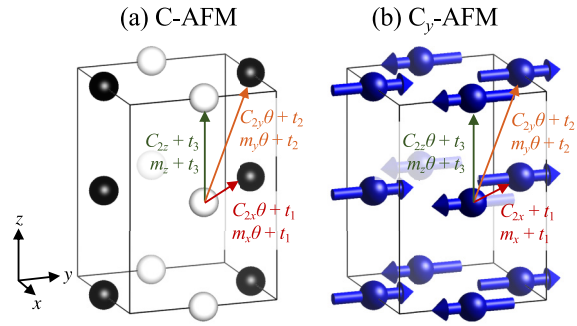

FIG. 6. Screw and glide symmetry operations in the (a) C-AFM configuration with black-and-white $Pb'n'm$ space group and the (b) C_y-AFM configuration with the magnetic $Pbn'm'$ space group. The translation vectors are shown by arrows; $t_1 = (\frac{1}{2}\frac{1}{2}0)$, $t_2 = (\frac{1}{2}\frac{1}{2}\frac{1}{2})$, and $t_3 = (00\frac{1}{2})$.

APPENDIX A: SYMMETRY ANALYSIS FOR SPIN SPLITTING

In the crystalline $Pbnm$ space group, there are eight symmetry operations: $\{E,\ I,\ C_{2x}+(\frac{1}{2}\frac{1}{2}0),\ C_{2y}+(\frac{1}{2}\frac{1}{2}\frac{1}{2}),\ C_{2z}+(00\frac{1}{2}),\ m_x+(\frac{1}{2}\frac{1}{2}0),\ m_y+(\frac{1}{2}\frac{1}{2}\frac{1}{2}),\ m_z+(00\frac{1}{2})\}$. Introducing the time-reversal symmetry θ and adding the products of θ and these eight symmetry operations, it will be the nonmagnetic $Pbnm1'$ space group having 16 symmetry operations. By considering an AFM order, the symmetry is reduced according to the spin configuration. When the SOC is not taken into account, the spin direction does not have the physical meaning, and the spin state shows just two states, i.e., up- and down-spin states. To treat the non-SOC magnetic symmetry, "*black-and-white group*" is sufficient [49]. As a matter of fact, the black-and-white group is often mixed up with the magnetic space group in the literature. Now we redefine it as follows. Figure 6(a) shows the C-AFM ordering where different spin sites are shown by black and white spheres. In the black-and-white group, rotation and mirror symmetry operations do not flip the spin, but only the time-reversal symmetry operation θ flips the spins as we turn over a black-and-white disk in the Reversi board game. Therefore, the black-and-white space group has eight symmetry operations: $\{E, I, C_{2z}+(00\frac{1}{2}), m_z+(00\frac{1}{2}), C_{2x}\theta+(\frac{1}{2}\frac{1}{2}0), C_{2y}\theta+(\frac{1}{2}\frac{1}{2}\frac{1}{2}), m_x\theta+(\frac{1}{2}\frac{1}{2}0), m_y\theta+(\frac{1}{2}\frac{1}{2}\frac{1}{2})\}$; we name it the black-and-white $Pb'n'm$ space group, and distinguish it from the magnetic $Pb'n'm$ space group that appeared in Table I despite the same name. Among those symmetry operations, the latter half accompanies spin-reversal symmetry θ and links the up-spin (black) sites and down-spin (white) sites, hence, making two spin states equivalent in the electronic state. In the k space, each k point has the little group of the black-and-white $Pb'n'm$ group, whereas the translation part in screw and glide operations is dropped. If the considered k point has one of

TABLE IV. Transformation property of the spin state s and the spin components (s_x, s_y, s_z) at the high-symmetric Γ, X, and S points and along the high-symmetric $\Gamma - X$ and $\Gamma - S$ lines in the orthorhombic Brillouin zone. Without the SOC, the C-AFM order follows black-and-white $Pb'n'm$ space group and with the SOC, the C_y-AFM order follows the magnetic $Pbn'm'$ space group. The possibility of spin splitting (ss) is shown at the last column.

Γ, X, S

C-AFM	E	I	C_{2z}	m_z	$C_{2x}\theta$	$C_{2y}\theta$	$m_x\theta$	$m_y\theta$	ss
s	1	1	1	1	−1	−1	−1	−1	no

Γ, X, S

C_y-AFM	E	I	C_{2x}	m_x	$C_{2y}\theta$	$C_{2z}\theta$	$m_y\theta$	$m_z\theta$	ss
s_x	1	1	1	1	1	1	1	1	yes
s_y	1	1	−1	−1	−1	1	−1	1	no
s_z	1	1	−1	−1	1	−1	1	−1	no

$\Gamma - X$

C-AFM	E	m_z	$C_{2x}\theta$	$m_y\theta$	ss
s	1	1	−1	−1	no

$\Gamma - S$

C-AFM	E	m_z	ss
s	1	1	yes

$\Gamma - X$

C_y-AFM	E	C_{2x}	$m_y\theta$	$m_z\theta$	ss
s_x	1	1	1	1	yes
s_y	1	−1	−1	1	no
s_z	1	−1	1	−1	no

$\Gamma - S$

C_y-AFM	E	$m_z\theta$	ss
s_x	1	1	yes
s_y	1	1	yes
s_z	1	−1	no

four symmetries : $\{C_{2x}\theta, C_{2y}\theta, m_x\theta, m_y\theta\}$ originating from the aforementioned screw and glide symmetries, it results in the spin degeneracy of the bands. Hereinafter, we call them "*spin-degenerate symmetry operations*" for the AFM order. Other symmetry operations in the space group, $\{E, I, C_{2z} + (00\frac{1}{2}), m_z + (00\frac{1}{2})\}$, link the same spin sites and do not cause the spin degeneracy. Obviously, in the FM order, there are no spin-degenerate symmetry operations and, hence, there is no spin degeneracy in the band structure.

Here, we demonstrate the symmetry analysis by taking band structure along the $\Gamma - X$ and the $\Gamma - S$ axes as examples; the X and S points are located at k=$(\frac{1}{2}, 0, 0)$ and $(\frac{1}{2}, \frac{1}{2}, 0)$ points in the Brillouin zone, respectively. Table IV shows the transformation properties of spin momenta along these lines. Without the SOC, it can be deduced that the $\Gamma - X$ line does not show the spin splitting whereas the $\Gamma - S$ line shows the spin splitting; the $\Gamma - S$ line holds m_z symmetry in the little group, but it is not the spin-degenerate symmetry operation. In other words, the spin state s is invariant under all the symmetry operations along the $\Gamma - S$ line. This was confirmed in our band-structure calculation shown in Figs. 7(a) and 7(c). It is interesting to see that the bands are spin degenerate between the Γ and the X points and largely spin split between the Γ and the S points without the help of SOC. This splitting originates from the AFM configuration that breaks the effective PT symmetry (i.e., product of the space-inversion and time-reversal symmetries) [46]. Recall that the spin considered here does not have any preferential direction but just black-and-white states.

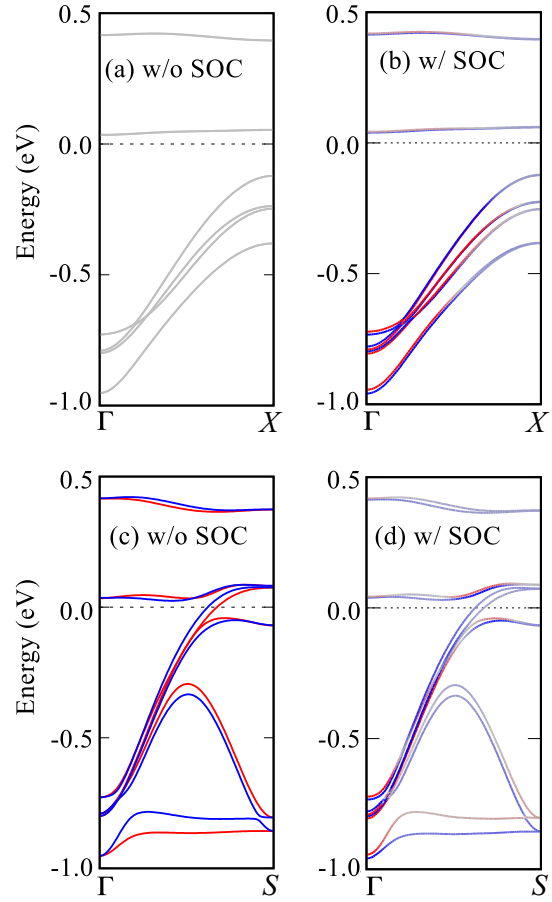

FIG. 7. Calculated band structure (a) and (b) along the $\Gamma - X$ line and (c) and (d) along the $\Gamma - S$ line in the orthogonal Brillouin zone. In (a) and (c), the SOC is turned off, and spin states are shown by red and blue colors. In (b) and (d), the SOC is turned on, and s_x polarization is shown by red and blue colors. Fermi energy is set as zero energy.

When SOC is turned on, the spin direction matters. Considering the spins as axial vectors, the mirror and rotation symmetry operations can flip the spin components (e.g., m_x mirror operation flips s_y and s_z but not s_x) as well as the time-reversal symmetry. By considering the C_y-AFM ordering, the nonmagnetic $Pbnm1'$ symmetry is reduced to be $Pbn'm'$ magnetic space group with eight symmetry operations : $\{E, I, C_{2x} + (\frac{1}{2}\frac{1}{2}0), m_x + (\frac{1}{2}\frac{1}{2}0), C_{2y}\theta + (\frac{1}{2}\frac{1}{2}\frac{1}{2}), C_{2z}\theta + (00\frac{1}{2}), m_y\theta + (\frac{1}{2}\frac{1}{2}\frac{1}{2}), m_z\theta + (00\frac{1}{2})\}$. In the C_y-AFM order, the spin momenta are collinearly aligned along the y direction and slightly canted towards the x direction. As shown in Table IV, the spin components s_x, s_y, s_z show different symmetry properties. Since the C_y-AFM order has the same irreducible representation as F_x order, s_x is invariant under all the symmetry operations; s_x polarization is allowed to arise everywhere in the k space as spin polarization in the FM order. Unlike the AFM-induced spin-splitting case, the magnitude of the spin splitting depends on the magnitude of the SOC in this case. As shown in Figs. 7(b) and 7(d), the band structure exhibits the additional small band splitting by the SOC on top of the non-SOC band structures [cf. Figs. 7(a) and 7(c)]. Along the $\Gamma - X$ axis, s_x polarization is induced by SOC

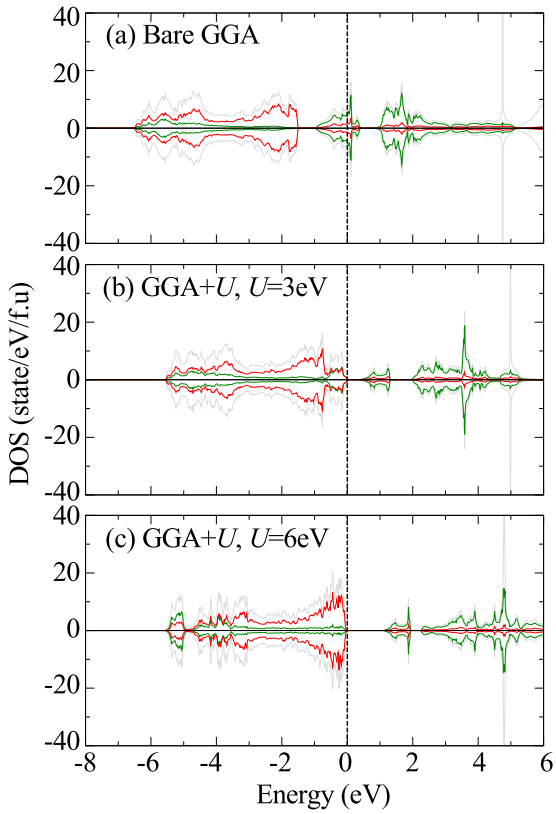

FIG. 8. Calculated total DOS (gray lines) with the GGA and GGA + U functionals with $U = 3$ and 6 eV in C-AFM $CaCrO_3$ without SOC. Projected DOSs onto Cr-d and O-p orbital states are also shown by green and red lines, respectively.

whereas s_y and s_z polarizations is still zero. Along the $\Gamma - S$ axis, s_x is induced by the SOC, and s_y is induced by the AFM order, whereas s_z is zero. Owing to the weak SOC interaction at the Cr 3d orbital state, the SOC-induced band splitting is much smaller than the AFM-induced splitting.

The same analysis can apply to the spin-splitting property discussed in Sec. D. Along the ΛH line, there are $\{E, m_x\theta\}$ symmetry operations originating from the black-and-white space group, and the latter protects the spin degeneracy of the band structure without SOC; the degeneracy is lifted by turning on the SOC because s_x polarization is allowed by $\{E, m_x\}$ symmetry originating from the magnetic space group as shown in Figs. 5(b) and 5(c). Along the nonsymmetric k line, all the spin polarization is allowed with/without the SOC as shown in Figs. 5(d) and 5(e). For further analysis, information on the other high-symmetric k points and their symmetry in the magnetic space group can be found in the Bilbao crystallographic server [50–52]. We confirmed that the spin degeneracy is symmetry protected along all the k paths in the band-structure plot in Fig. 1(c) without the SOC. body.

TABLE V. Relative total energy (meV/f.u) calculated with the GGA and GGA+U functionals with $U = 3$ and $U = 6$ eV for several spin configurations: FM, A-, C-, and G-type AFM configurations. The lowest energy is highlighted. The crystal structure (both the lattice parameters and the atomic coordinates) was relaxed under the C-AFM order, and then the total energy was compared by using the VASP code with 12 × 12 × 10 k-point mesh.

ΔE (meV/f.u)	FM	A-AFM	C-AFM	G-AFM
Bare GGA	209.2	59.4	**0**	103.9
GGA+U (U=3 eV)	**0**	12.6	57.5	17.2
GGA+U (U=6 eV)	**0**	61.8	52.3	52.9

APPENDIX B: EFFECT OF HUBBARD U CORRECTION

In strongly correlated materials, the Hubbard U correction of the DFT + U approach is widely used to reinforce the on-site Coulomb repulsion for 3d- or 4f-localized orbital states [53]. Figure 8 shows the change in the electronic state in $CaCrO_3$ with the GGA and GGA + U potentials with various U values. At the bare GGA level (with $U = 0$ eV), the Fermi level crosses the Cr-t_{2g} orbital state showing the good metallic state. As increasing the U value, we found the band-gap opening with $U \gtrsim 2.5$ eV. The band gap increases from 0.3 eV at $U = 3$ to 1.0 eV at $U = 6$ eV. This is consistent with the result reported by Streltsov *et al.*; the electronic state is metallic at the local spin density approximation (LSDA) level and insulating at the LSDA + U level [32]. Nevertheless, the GGA + U result is inconsistent with the experimental observations of metallicity in $CaCrO_3$ [21]. Table V shows the relative total energy for four magnetic configurations with several U values. The bare GGA result correctly reproduces the C-AFM ground state, consistent with the experiment, whereas GGA + U results show the wrong solution as the FM ground state. In fact, the Hubbard U correction often overestimates the tendency toward ferromagnetism as already noted in previous DFT studies on orthorhombic rare-earth manganites [54,55]. Considering the better description of the metallic state and the magnetic stability, the bare GGA functional was used in our DFT calculation.

[1] R. Karplus and J. M. Luttinger, Phys. Rev. **95**, 1154 (1954).
[2] H. Chen, Q. Niu, and A. H. MacDonald, Phys. Rev. Lett. **112**, 017205 (2014).
[3] J. Kübler and C. Felser, Europhys. Lett. **108**, 67001 (2014).
[4] H. Yang, Y. Sun, Y. Zhang, W.-J. Shi, S. S. P. Parkin, and B. Yan, New J. Phys. **19**, 015008 (2017).
[5] Y. Zhang, Y. Sun, H. Yang, J. Železný, S. P. P. Parkin, C. Felser, and B. Yan, Phys. Rev. B **95**, 075128 (2017).
[6] S. Nakatsuji, N. Kiyohara, and T. Higo, Nature (London) **527**, 212 (2015).
[7] N. Kiyohara, T. Tomita, and S. Nakatsuji, Phys. Rev. Appl. **5**, 064009 (2016).
[8] A. K. Nayak, J. E. Fischer, Y. Sun, B. Yan, J. Karel, A. C. Komarek, C. Shekhar, N. Kumar, W. Schnelle, J. Kübler, C. Felser, and S. S. P. Parkin, Sci. Adv. **2**, e1501870 (2016).
[9] J.-Y. Yoon, Y. Takeuchi, S. DuttaGupta, Y. Yamane, S. Kanai, J. Ieda, H. Ohno, and S. Fukami, AIP Adv. **11**, 065318 (2021).

[10] T. Chen, T. Tomita, S. Minami, M. Fu, T. Koretsune, M. Kitatani, I. Muhammad, D. Nishio-Hamane, R. Ishii, F. Ishii, R. Arita, and S. Nakatsuji, Nat. Commun. **12**, 572 (2021).

[11] R. Shindou and N. Nagaosa, Phys. Rev. Lett. **87**, 116801 (2001).

[12] W. Shi, L. Muechler, K. Manna, Y. Zhang, K. Koepernik, R. Car, J. van den Brink, C. Felser, and Y. Sun, Phys. Rev. B **97**, 060406(R) (2018).

[13] L. Šmejkal, R. González-Hernández, T. Jungwirth, and J. Sinova, Sci. Adv. **6**, eaaz8809 (2020).

[14] K. Samanta, M. Ležaić, M. Merte, F. Freimuth, S. Blügel, and Y. Mokrousov, J. Appl. Phys. **127**, 213904 (2020).

[15] X. Li, A. H. MacDonald, and H. Chen, Quantum anomalous hall effect through canted antiferromagnetism, arXiv:1902.10650.

[16] M.-T. Suzuki, T. Koretsune, M. Ochi, and R. Arita, Phys. Rev. B **95**, 094406 (2017).

[17] V. T. N. Huyen, M.-T. Suzuki, K. Yamauchi, and T. Oguchi, Phys. Rev. B **100**, 094426 (2019).

[18] D. Vanderbilt, *Berry Phases in Electronic Structure Theory* (Cambridge University Press, Cambridge, 2018).

[19] M. Naka, Y. Motome, and H. Seo, Phys. Rev. B **106**, 195149 (2022).

[20] J. Goodenough, J. Longo, and J. Kafalas, Mater. Res. Bull. **3**, 471 (1968).

[21] J.-S. Zhou, C.-Q. Jin, Y.-W. Long, L.-X. Yang, and J. B. Goodenough, Phys. Rev. Lett. **96**, 046408 (2006).

[22] E. Castillo-Martínez, A. Durán, and M. Alario-Franco, J. Solid State Chem. **181**, 895 (2008).

[23] J. Weiher, B. Chamberland, and J. Gillson, J. Solid State Chem. **3**, 529 (1971).

[24] A. C. Komarek, S. V. Streltsov, M. Isobe, T. Möller, M. Hoelzel, A. Senyshyn, D. Trots, M. T. Fernández-Díaz, T. Hansen, H. Gotou, T. Yagi, Y. Ueda, V. I. Anisimov, M. Grüninger, D. I. Khomskii, and M. Braden, Phys. Rev. Lett. **101**, 167204 (2008).

[25] O. Ofer, J. Sugiyama, M. Månsson, K. H. Chow, E. J. Ansaldo, J. H. Brewer, M. Isobe, and Y. Ueda, Phys. Rev. B **81**, 184405 (2010).

[26] G. Kresse and J. Furthmüller, Phys. Rev. B **54**, 11169 (1996).

[27] P. Giannozzi, S. Baroni, N. Bonini, M. Calandra, R. Car, C. Cavazzoni, D. Ceresoli, G. L. Chiarotti, M. Cococcioni, I. Dabo, A. D. Corso, S. de Gironcoli, S. Fabris, G. Fratesi, R. Gebauer, U. Gerstmann, C. Gougoussis, A. Kokalj, M. Lazzeri, L. Martin-Samos *et al.*, and J. Phys.: Condens. Matter **21**, 395502 (2009).

[28] J. P. Perdew, K. Burke, and M. Ernzerhof, Phys. Rev. Lett. **77**, 3865 (1996).

[29] P. E. Blöchl, Phys. Rev. B **50**, 17953 (1994).

[30] A. Dal Corso, Comput. Mater. Sci. **95**, 337 (2014).

[31] A. A. Mostofi, J. R. Yates, Y.-S. Lee, I. Souza, D. Vanderbilt, and N. Marzari, Comput. Phys. Commun. **178**, 685 (2008).

[32] S. V. Streltsov, M. A. Korotin, V. I. Anisimov, and D. I. Khomskii, Phys. Rev. B **78**, 054425 (2008).

[33] H. M. Liu, C. Zhu, C. Y. Ma, S. Dong, and J.-M. Liu, J. Appl. Phys. **110**, 073701 (2011).

[34] Y. Quan, V. Taufour, and W. E. Pickett, Phys. Rev. B **105**, 064517 (2022).

[35] A. Leonhardt, M. M. Hirschmann, N. Heinsdorf, X. Wu, D. H. Fabini, and A. P. Schnyder, Phys. Rev. Mater. **5**, 124202 (2021).

[36] D. Treves, Phys. Rev. **125**, 1843 (1962).

[37] E. F. Bertaut, Acta Crystallogr., Sect. A: Cryst. Phys., Diffr., Theor. Gen. Crystallogr. **24**, 217 (1968).

[38] I. V. Solovyev, Phys. Rev. B **55**, 8060 (1997).

[39] B. J. Campbell, H. T. Stokes, D. E. Tanner, and D. M. Hatch, J. Appl. Crystallogr. **39**, 607 (2006).

[40] X. Wang, J. R. Yates, I. Souza, and D. Vanderbilt, Phys. Rev. B **74**, 195118 (2006).

[41] M. G. Lopez, D. Vanderbilt, T. Thonhauser, and I. Souza, Phys. Rev. B **85**, 014435 (2012).

[42] We obtained a larger AHC value in FM order; $\sigma_{yz} = -150$ S/cm with F_x order in $CaCrO_3$.

[43] Y. Yao, L. Kleinman, A. H. MacDonald, J. Sinova, T. Jungwirth, D.-S. Wang, E. Wang, and Q. Niu, Phys. Rev. Lett. **92**, 037204 (2004).

[44] X. Wang, D. Vanderbilt, J. R. Yates, and I. Souza, Phys. Rev. B **76**, 195109 (2007).

[45] F. D. M. Haldane, Phys. Rev. Lett. **93**, 206602 (2004).

[46] L.-D. Yuan, Z. Wang, J.-W. Luo, and A. Zunger, Phys. Rev. Mater. **5**, 014409 (2021).

[47] A. C. Komarek, T. Möller, M. Isobe, Y. Drees, H. Ulbrich, M. Azuma, M. T. Fernández-Díaz, A. Senyshyn, M. Hoelzel, G. André, Y. Ueda, M. Grüninger, and M. Braden, Phys. Rev. B **84**, 125114 (2011).

[48] K. Momma and F. Izumi, J. Appl. Crystallogr. **44**, 1272 (2011).

[49] G. Burns, *Introduction to Group Theory with Applications* (Academic, New York, 1977).

[50] M. I. Aroyo, J. M. Perez-Mato, D. Orobengoa, E. M. R. E. Tasci, G. de la Flor, and A. Kirov, Bulg. Chem. Commun. **43**, 183 (2011).

[51] M. I. Aroyo, J. M. Perez-Mato, C. Capillas, E. Kroumova, S. Ivantchev, G. Madariaga, A. Kirov, and H. Wondratschek, Z.Kristallogra.-Crystal. Mater. **221**, 15 (2006).

[52] M. I. Aroyo, A. Kirov, C. Capillas, J. M. Perez-Mato, and H. Wondratschek, Acta Crystallogr., Sect. A: Found. Crystallogr. **62**, 115 (2006).

[53] S. L. Dudarev, G. A. Botton, S. Y. Savrasov, C. J. Humphreys, and A. P. Sutton, Phys. Rev. B **57**, 1505 (1998).

[54] I. Solovyev, N. Hamada, and K. Terakura, Phys. Rev. B **53**, 7158 (1996).

[55] S. Picozzi, K. Yamauchi, G. Bihlmayer, and S. Blügel, Phys. Rev. B **74**, 094402 (2006).